Proceedings of the Project Review, Geo-Mathematical Imaging Group (Purdue University, West Lafayette IN), Vol. 1 (2008) pp. 203-220.

LABORATORY-SCALE STUDY OF FIELD-OF-VIEW AND THE SEISMIC INTERPRETATION OF FRACTURE SPECIFIC STIFFNESS

ANGEL ACOSTA-COLON*, LAURA J. PYRAK-NOLTE†, AND DAVID D. NOLTE‡

Abstract. The effects of the scale of measurement, i.e., the field-of-view, on the interpretation of fracture properties from seismic wave propagation was investigated using an acoustic lens system to produce pseudo-collimated wavefronts. The incident wavefront had a controllable beam diameter that set the field-of-view at 15 mm, 30 mm and 60 mm. At a smaller scale, traditional acoustic scans were used to probe the fracture in 2 mm increments. This laboratory approach was applied to two limestone samples, each containing a single induced fracture, and compared to an acrylic control sample. From the analysis of the average coherent sum of the signals measured on each scale, we observed that the scale of the field-of-view affected the interpretation of fracture specific stiffness. Many small-scale measurements of the seismic response of a fracture, when summed, did not predict the large-scale response of the fracture. The change from a frequency-independent to a frequency-dependent fracture stiffness occurs when the scale of the field-of-view exceeds the spatial correlation length associated with fracture geometry. A frequency-independent fracture specific stiffness is not sufficient to classify a fracture as homogeneous. A non-uniform spatial distribution of fracture specific stiffness and overlapping geometric scales in a fracture cause a scale-dependent seismic response which requires measurements at different field-of-views to fully characterize the fracture.

1. Introduction. The scaling behavior of the hydraulic and seismic properties of a fracture determines how properties observed on the laboratory size (typically less than tens of cm) relate to the same properties measured at larger sizes. In describing the scaling behavior of fracture properties, the length scales of the fracture geometry (apertures, contact areas, spatial correlations), fluid phase distribution (wetting and non-wetting phase areas, interfacial areas), must be characterized and compared to the length scales associated with the seismic probe (wavelength, beam size, divergence angle, field-of-view).

For fractures in rock, measurements on the laboratory scale encompass several different length scales that include the size of the sample and the size of the fracture. A single fracture can be viewed as two rough surfaces in contact that produce regions of contact and open voids in a quasi-two-dimensional fashion. This fracture geometry has many length scales that are described contact area and its spatial distribution, as well as by the size (aperture) and spatial distribution of the void space. From laboratory measurements, Pyrak-Nolte et al. (1997) [1] found that the aperture distribution of natural fracture networks in whole-drill coal cores were spatially correlated over 10 mm to 30 mm, i.e., distances that were comparable to the size of the core samples. However, asperities on natural joint surfaces have been observed to be correlated over only about 0.5 mm [2] from surface roughness measurements. These two quoted values for correlation lengths vary by up to two orders of magnitude. The spatial correlation lengths are likely to be a function of rock type, but this needs to be verified experimentally. The observation that correlation lengths are smaller or on the same order as the sample size may explain why core samples often predict different hydraulic-mechanical behavior than is observed in the field. If a fracture on the core scale is correlated over a few centimeters, the same fracture on the field scale may behave as an uncorrelated fracture.

An additional length scale that is necessary to consider when investigating the scaling behavior of seismic wave propagation across single fractures is the spatial variation in fracture specific stiffness. Fracture specific stiffness is defined as the ratio of the increment of stress to the increment of displacement caused by the deformation of the void space in the fracture. As stress on the fracture increases, the contact area between the two fracture surfaces also increases, raising the stiffness of the fracture. Fracture specific stiffness depends on the elastic properties of the rock and depends critically on the amount and distribution of contact area in a fracture that arises from two rough surfaces in contact [3-5]. Kendall & Tabor [6] showed experimentally and Hopkins et al. [4,5]

*Department of Earth and Atmospheric Sciences, Purdue University, West Lafayette, Indiana 47907 (aacostate@purdue.edu).

†Department of Physics, Purdue University, West Lafayette, Indiana 47907, Department of Earth and Atmospheric Sciences, Purdue University, West Lafayette, Indiana 47907 (ljpn@physics.purdue.edu).

‡Department of Physics, Purdue University, West Lafayette, Indiana 47907 (nolte@physics.purdue.edu).

have shown numerically that interfaces with the same amount of contact area but different spatial distributions of the contact area have different stiffnesses. Greater separation between points of contacts results in a more compliant fracture or interface.

The geometric length scales of a fracture affect the length scales involved in the flow of multiple fluid phases in a fracture partially saturated with gas and water. Recently, Johnson et al. [7] showed experimentally and numerically that for intersecting fractures fluid-fluid mixing in intersecting fractures is controlled by the spatial correlations of the aperture distributions in the fractures. Pyrak-Nolte & Morris [8] found that spatial correlations of the fracture apertures control the relationship between fluid flow through a fracture and fracture specific stiffness. Furthermore, the fracture void geometry is sensitive to stress as well as chemical alteration through precipitation and dissolution, and also controls the distribution of multiple fluid phases (e.g. gas and water) leading to interfacial area per volume (IAV) which is an inverse length scale. These physical processes have the potential to alter the geometric length scales of a fracture.

All of these geometric length scales can be compared to the wavelength of the seismic probe, as well as to the scale sampled by the seismic probe. In terms of seismic monitoring of fractures, the role of size and spatial distributions of fracture stiffness distributions are determined by the wavelength of the signal and by the size of the region probed. Pyrak-Nolte & Nolte [9] showed theoretically that, for a single fracture, different wavelengths sample different subsets of fracture geometry. They calculated dynamic fracture stiffness based on the displacement discontinuity theory [10-12] for wave transmission across a fracture. Transmission was based on local stiffnesses. A uniform distribution results in a frequency-independent dynamic fracture specific stiffness. A biomodal distribution results in a dynamic stiffness that depends weakly on frequency. However, a strongly inhomogenous distribution of fracture specific stiffness results in a frequency-dependent fracture specific stiffness. The increase in dynamic stiffness with increasing frequency reflects the change in the subset of fracture geometry that is being sampled at a particular wavelength. Thus, when interpreting fracture specific stiffness from seismic measurements, the dependence of stiffness on wavelength gives an indication of the length scales associated with fracture geometry (i.e., contact area, aperture, fracture specific stiffness) relative to the wavelength.

The theoretical work of Pyrak-Nolte & Nolte [9] only explored the effect of spatially uncorrelated distributions of fracture specific stiffness on seismic wave transmission. However, one must also consider the effect of spatial correlations on the interpretation of seismic measurements. Whether working on the laboratory scale or on the field scale, seismic measurements only probe a portion of a fracture (local measurement). The area illuminated by the wavefront is a function of the wavelength as well as the source-receiver configurations. In laboratory studies, the lateral size of the acoustic lobe pattern at the fracture plane determines the region sampled with traditional contact transducers. The first-order effect of spatial correlations of fracture specific stiffness is that local seismic measurements sample different fracture specific stiffnesses in different regions of the fracture. The second-order effect of a spatially-varying fracture specific stiffness is scattering caused by a heterogeneous distribution of fracture specific stiffness. The strength of the scattering depends on the spatial correlation length of the variation in fracture specific stiffness relative to a wavelength, and on the field-of-view of the seismic measurements. A fundamental question is whether the size of the region probed is sufficient to capture high-angle scattering losses outside of the detection angle. If scattering angles are high, this raises the important question of how many seismic measurements are needed to fully characterize a fracture. To begin to answers such questions, the effect of field-of-view on the interpretation of fracture specific stiffness from seismic measurements needs to be explored. This paper presents results of a laboratory study that examines the effect of field-of-view on the interpretation of fracture specific stiffness from seismic measurements.

2. Experimental Methods. Two experimental approaches were used to measure the seismic signature of a fracture. These methods are: (1) an acoustic lens system, and (2) an acoustic mapping system. With the acoustic lens system, the area illuminated by the seismic wavefront is varied to change the field-of-view (i.e., the region probed by the wavefront). This approach enables

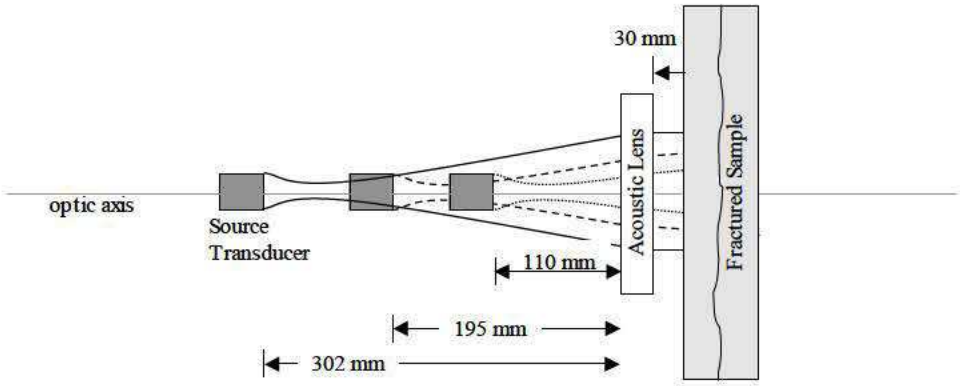

FIG. 1. *Sketch of the experimental set-up to create pseudo-collimated acoustic beams with beam waists measuring approximately 60 mm (solid line), 30 mm (dashed line) and 15 mm (dotted line) using a spherically-focused source transducer and an acoustic lens. The distance between the source transducer and the acoustic lens is adjusted to vary the beam size at the surface of the sample.*

us to investigate the effect of field-of-view on the interpretation of fracture properties from seismic measurements. In the next section, a brief discussion of the design and characterization of the lens system is provided. The second approach, acoustic mapping, produces a high-resolution map of the local variations in fracture properties over a two-dimensional region. Both experimental approaches were used to explore the interpretation of fracture specific stiffness from seismic measurements as a function of field-of-view and as a function of seismic frequency.

2.1. Acoustic Lens System. For this study, an acoustic lens system was designed to produce pseudo-collimated beams with adjus0.2in probe diameters, shown in Figure 1. The area illuminated by the seismic wavefront was varied to change the field-of-view (i.e., the region probed by the wavefront). The acoustic lens was designed using geometric optics of elliptical lenses. An elliptical surface (Figure 2) was chosen to eliminate on-axis aberration [13]. The side of the lens facing the transducer had a concave ellipsoidal surface (concave meniscus) and the side of the lens facing the sample was flat. The geometrical shape of the ellipsoid is determined by the semi major axis (a), semi minor axis (b) and the center of the ellipsoid (c). For machining purposes, the ellipsoid was represented by a sphere with a curvature matched to the ellipsoid. The sphere has a radius R_1 and centered at a point such that the sphere surface matches the apex of the elliptical surface, as shown in Figure 2. The lens dimensions are the diameter (d) and the length (l) from the apex of the lens to the flat surface. Because the lens is submerged in water during data acquisition, the acoustic impedance and the matching impedance of water were used for the design. This avoids large dispersion and a large angles of refraction created by the different material properties.

The material for the lens was acrylic (Lucite). Table 2.1 lists the properties of Lucite and water. The lenses were right cylinders of acrylic measuring 80 mm in diameter (d) by 25.4 mm in length (l). The diameter of the lens was chosen to be 80 mm because the maximum diameters of the collimated wavefront are limited to the diameter of the lens. The 25.4 mm length was chosen for ease of machining. The spherical radius R_1 depends on a and b. Calculation of the radius of curvature R_1 is obtained by using the equation for an ellipse,

$$\frac{x^2}{a^2} + \frac{y^2}{b^2} = 1. \tag{2.1}$$

By taking the second derivative of the ellipse equation with respect to y, the radius of curvature is

$$R_1 = \frac{b^2}{a} \tag{2.2}$$

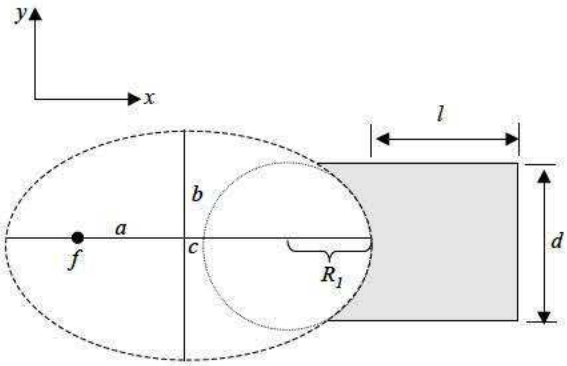

FIG. 2. *Sketch of the geometry to create the acoustic lens.*

	Water	Lucite
Acoustic Velocity (m/s)	1480	2730
Acoustic Impedance ($\times 10^6$ kg/m^2)	1.48	3.22

TABLE 2.1
Acoustic Properties of water, Lucite (acrylic) and steel.

The focal length of the lens used for the experiments was chosen to accept the largest beam width of 60 mm and to collimate the beam through the fracture. The focal point of the lens was set by

$$f = \frac{D}{2\tan\alpha} \tag{2.3}$$

where D is the desired diameter of the collimated wavefront and α is the half angle of the diverge of the wavefront from the transducer at it's focal point (not the lens). The divergence angle (α) of the transducer is 5°. For a beam diameter of 60 mm, the focal length is $f = 310$ mm. This focal length determines R_1 using the index of refraction of water (n_w) and Lucite (n_l) as

$$f = \frac{n_w}{n_l - n_w} R_1 = \frac{R_1}{n-1} \tag{2.4}$$

where the index of refraction in acoustics is the inverse of the velocity of sound in the material. The radius is then

$$R_1 = (n-1)f \tag{2.5}$$

where $n = 0.54$ for water and lucite. The lens radius for the 60 mm beam diameter was 143 mm (see Table 2.2 for the value of the other parameters).

The lens that was designed to collimate the 60 mm diameter beam also was used to produce a 30 mm and a 15 mm pseudo-collimated beam diameter at the fracture plane. These smaller beam diameters were produced by moving the transducer closer to the lens. The lens intersects the diverging beam when the beam is smaller and directs it towards the fracture. The distances L of the transducer from the lens to produce these beam diameters, shown in Figure 1, were 302 mm (for 60 mm), 195 mm (for 30 mm) and 110 (for 15 mm). The beam diameters were verified by scanning a transducer across the beam at a distance equivalent to the distance of the fracture from the lens.

Design	Value
R_1	143.02mm
a	202.52mm
b	170.19mm
l	25.4mm
d	80mm
material	Lucite

TABLE 2.2
Values for the design of the acoustic lens.

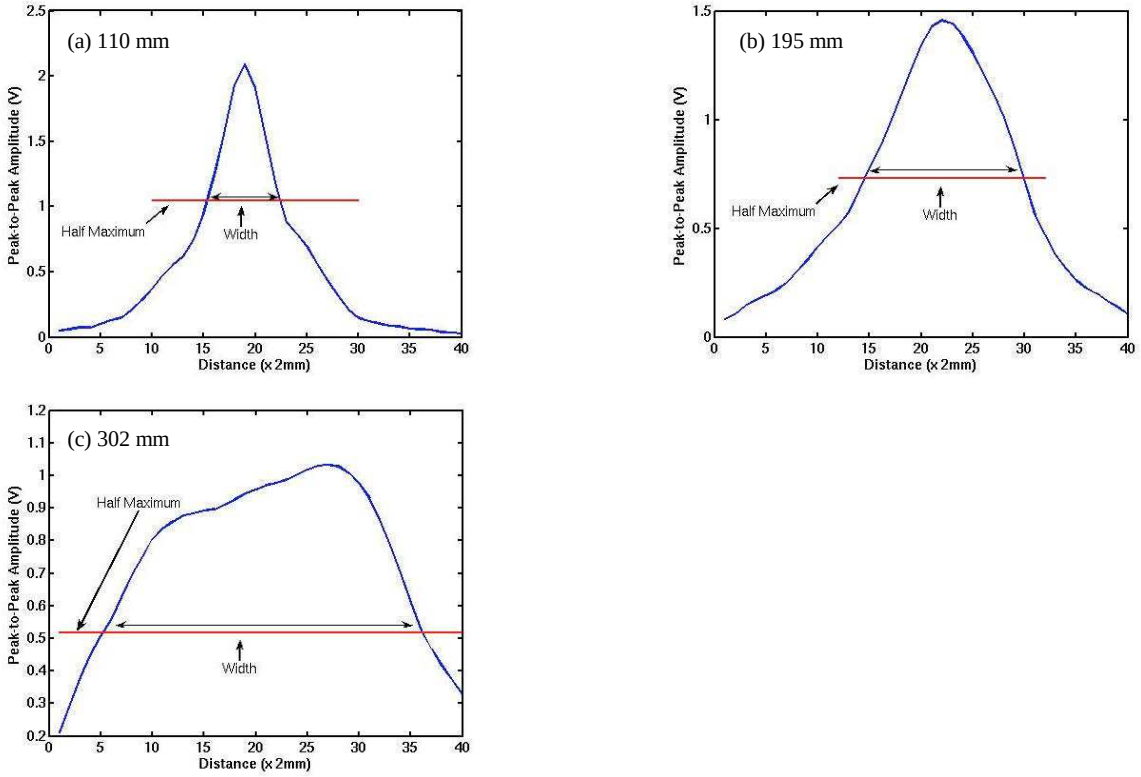

FIG. 3. *Beam profiles measured 65 mm from the surface of the acoustic lens for source - lens separations of (a) 110 mm, (b) 195 mm and (c) 302 mm. Using the full width at half max, the diameters of the beam waists are (a) 15 mm, (b) 30 mm and (c) 60 mm. The variation in arrival time across the beam waist is listed in Table 2.3.*

The beam profile measurements are shown in Figure 3. The beam diameters ere taken as the full width at half max.

The collimation of these smaller beams was not exact, because the transducer is moved toward the lens from the focal point for each of these cases, and hence the beams were diverging at the location of the fracture. The degree of non-collimation for the 30 mm and 15 mm beam diameters can be estimated by considering the depth of focus (twice the Rayleigh range) of the beam passing through the lens. If the distance of the source point to the lens is within a Rayleigh range, then the beam leaving the lens will be nearly collimated. The Rayleigh range of the beams is given by

L (mm)	Field-of-View (mm)	Variation in Arrival Time (μs)	Error (%)
110	15	0.20	4.1
195	30	0.19	6.4
302	60	0.37	5.0

TABLE 2.3

Distance between source and lens (L), the resulting field-of-view, the variation in arrival time across the pseudo-collimated wavefront, and the percent error in measured transmitted amplitude.

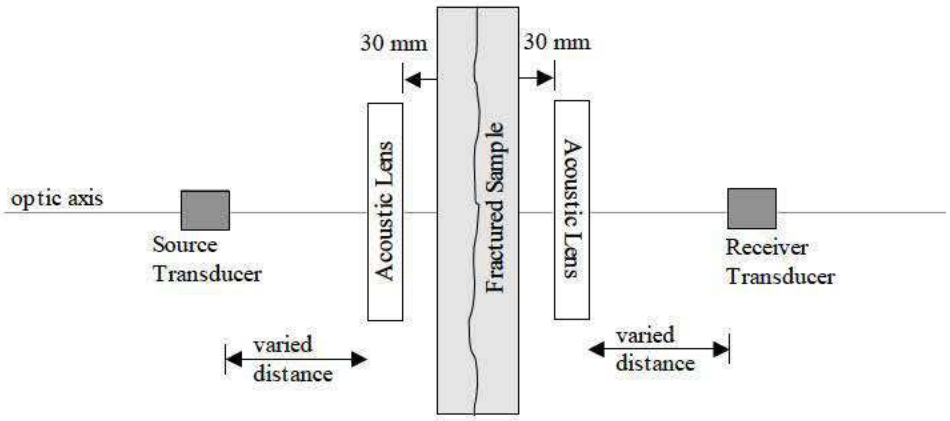

FIG. 4. *Sketch of the acoustic lens system experimental set-up to to obtain the seismic measurements as a function of field-of-view. The distance between the transducers and the lens were the same for the source side of the sample and the receiver side of the sample. The distances used are listed in Table 2.3.*

$$Z_R = \frac{4}{\pi}\frac{f^2\lambda}{D^2} \tag{2.6}$$

where D is the beam diameter. The Rayleigh ranges Z_R for the three beam diameters are equal to 124 mm (for 60 mm), 496 mm (for 30 mm) and 2000 mm (for 15 mm). The Rayleigh ranges for the 30 mm and 15 mm diameter probe beams are much larger than the source-to-lens distance (because the beam diameters are no more than ten times the wavelength). Therefore, the use of the lens designed to collimate the 60 mm diameter beam also produces pseudo-collimated beams in the other two cases of 30 mm and 15 mm. This near-collimation is confirmed by the small variation of the arrival time across the beam at the location of the fracture as listed in Table 2.3.

Two acoustic lenses were used in the acoustic system, one on the source side, and one symmetrically on the receiver side to collect the transmitted waves, as shown in Figure 4. The source transducer was a compressional-mode water-coupled spherically-focused piezoelectric transducer (central frequency of 1 MHz) and the receiver was a water-coupled plane-wave transducer (central frequency of 1 MHz) with a 2 mm pinhole on the receiver face. The pinhole was used to obtain a "point" measurement. The water coupling ensured reliable coupling between the sample and transducer for the acoustic mapping method. The receiver transducer location was matched to the source locations.

Because the locations of the source and receiver transducers were not at the focal planes of the lenses in our experimental configuration for the 30 mm and 15 mm beam diameters, it is necessary to assess if the field-of-view is restricted relative to the probe beam size by vignetting. Vignetting would be significant in the ray optics regime for Fresnel numbers much larger than unity. The Fresnel number for the beams is given by

$$N_F = \frac{D^2}{L\lambda} \tag{2.7}$$

where L is the distance from the lens to the receiver. The Fresnel numbers N_F are equal to 1.1 (for 60 mm), 1.8 (for 30 mm) and 4.4 (for 15 mm). These Fresnel numbers are comparable to unity, demonstrating that no significant vignetting (restriction on the field of view) occurs in our system design despite the locations of the transducers off of the focal planes. The fact that the Fresnel numbers are all near unity indicates that the laboratory lens system is operating in the transition between the near-field and the far-field. Fresnel numbers near unity also indicate that diffration effects are strong, and the ray approximation cannot be used.

A related analysis calculates the spatial blurring (Fresnel length) at the fracture plane as viewed by the receiver transducer through the collecting lens. If the Fresnel length is larger than or comparable to the beam size, then the field of view is set by the beam size and no, or little, vignetting occurs. The Fresnel length observed by the receiving transducer is given by

$$\xi_F = \sqrt{\frac{Lf\lambda}{f-L}} \tag{2.8}$$

In the three cases, the Fresnel lengths are 77 mm (for 60 mm), 33 mm (for 30 mm) and 17 mm (for 15 mm). The Fresnel lengths are comparable to the beam sizes, confirming that vignetting is not significantly reducing the field-of-view relative to the beam size. Furthermore, even if a small amount of vignetting is occuring, the similarity of the ratios of the Fresnel length to the beam diameter for all three cases indicates that each is affected almost equally. Therefore, for all three beam diameters, the field-of-view observed by the pin-hole at the receiving transducer is set approximately by the designed probe beam sizes of 60 mm, 30 mm and 15 mm.

For the desired beam diameters of 15 mm, 30 mm and 60 mm, the sampling pattern shown in Figure 5 was used. For the 60 mm field-of-view, one measurement was made at the center of the sample. For the 30 mm field-of-view, four measurements were made that covered the same approximate region. For the 15 mm field-of-view, 16 measurements were made as shown in Figure 5. Computer-controlled linear actuators were used to move the sample to collect the data for the 15 mm and 30 mm probe sizes.

2.2. Acoustic Mapping Method. The second approach used to probe fracture properties was an acoustic mapping method. Acoustic mapping (C-scans) probed the same 80 mm by 80 mm area of the fracture in 2 mm increments. Figure 5 shows the region (square area) over which the acoustic method mapping was applied to the sample relative to the measurements made for the three probe sizes. Computer-controlled linear actuators were used to move the source and receiver in unison. In the text and in the Figures, we refer to data obtained from the acoustic map as the 2 mm scale, because the receiving transducer used a 2 mm aluminum pinhole plate. The transducers were oriented perpendicular to the surface of the sample and were coaxially aligned. The distance of the acoustic mapping transducers from the face of the sample was 30 mm. The experimental setup was similar to that of the acoustic lens system, but instead of the lenses the transducers were located where the acoustic lenses are located in Figure 4. The acoustic mapping datasets consist of a 20 microseconds window of 1600 waveforms that contain the compressional wave (first arrival) to obtain the local variations in the seismic response of the fracture.

2.3. Sample Preparation. Two limestone rock samples (Rock 1 & Rock 2), each containing a single induced fracture, and one acrylic control sample (Intact) were used in this study. The control sample (Intact) did not contain any fractures and was used to measure systematic trends. All three samples were right cylinders with a diameter of 156 mm. The height of samples Rock 1, Rock 2 and Intact were 72 mm, 76 mm and 68 mm, respectively. A fracture was induced in Rock 1 and Rock

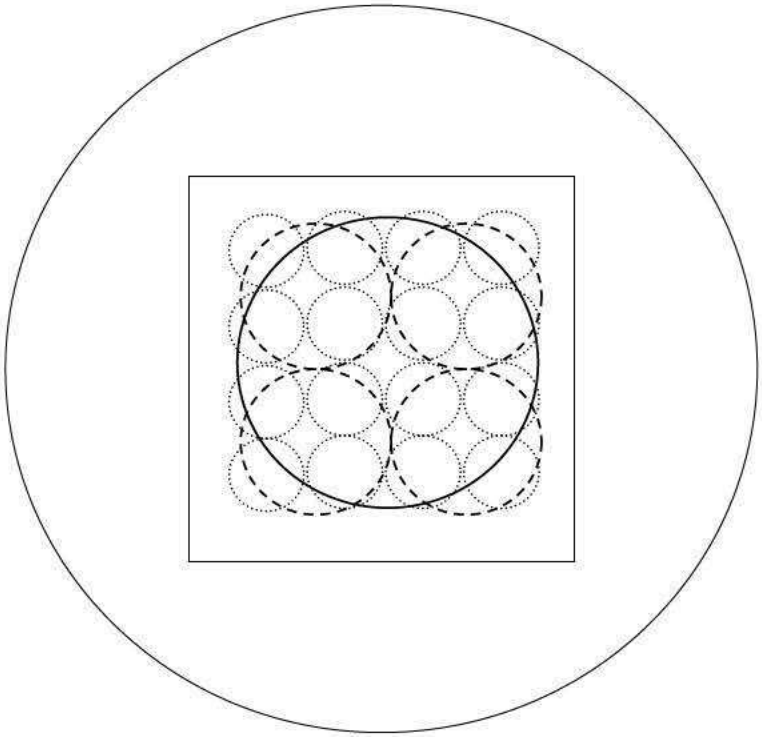

FIG. 5. *A sketch of the regions probed for different field-of-views relative to the sample diameter (156 mm). Sixteen regions were probed for the 15 mm (dotted-edged circles) field-ofview; four regions for the 30 mm (dashed-edged circles) field-of-view; and one region for the 60 mm (solid-edged circle) field-of-view. The sqaure region represents the area probed using the acoustic mapping method, i.e. measurements were made in 2 mm increments over an 80 mm by 80 mm area.*

2 using a technique similar to the Brazil testing [14]. After fracturing of the limestone samples, inlet and outlet ports were attached to the sample for flow measurements and for the injection of reactive fluids as well as sand transport (silica beads). Rock 1 had two ports (180° apart), while Rock 2 was fitted with eight ports (45° apart). The samples were sealed with marine epoxy to avoid geochemical interaction between the surface of the rock and the water in the acoustic imaging tank. The same seismic measurements were performed on the Intact sample as were performed on Rock 1 and Rock 2. For the initial measurements (i.e. initial condition) of the limestone samples, the samples were vacuum-saturated with water.

2.4. Alteration of Sample. Two different processes were used to alter the fractures in the rock samples to change the fracture specific stiffness through non-mechanical processes: 1) reactive flow that produced chemical alteration of the fracture, and 2) simulated sand transport by using silica beads. The reactive flow altered the fracture geometry by etching and/or precipitating minerals in the limestone. Sand transport was used to deposit and/or erode the fractures. Seismic and flow-rate measurements were made before and after each alteration. A falling-head method was used to obtain the flow rates through the fracture plane. The measurements for the initial water-saturated fracture condition without any alterations are referred to as *initial*. For Rock 1, an aqueous solution of 30% hydrochloric acid (HCl) was used, which was the *final* condition for Rock 1. For Rock 2, a reactive solution of HCl and sulfuric acid (H_2SO_4) solution was used followed by a silica bead flow. For Rock 2, the seismic and flow measurements after the chemical flow are referred to as *reactive* and after the silica bead flow is referred to as the *final* condition.

2.5. Chemical Alteration and Sand Transport. The limestone-fractured samples (Rock

1 and Rock 2) were subjected to chemical alteration. Limestone is a sedimentary rock composed primarily of the mineral calcite. For Rock 1, the aqueous HCl solution resulted in the dissolution of calcite (calcium carbonate, $CaCO_3$) and the production of calcium chloride ($CaCl_2$)

$$CaCO_3(s) + 2HCl(aq) \Rightarrow CaCl_2(aq) + CO_2(g) + H_2O.$$

For Rock 2, the chemical solution consisted of a combination of 0.24 M HCl and 0.36 M H_2SO_4 [15]. The sulfuric acid (H_2SO_4) reacts with the limestone producing the mineral gypsum ($CaSO_4$) and carbon dioxide and water,

$$H_2SO_4(aq) + CaCo_3(s) \Rightarrow CaSO_4(s) + CO_2(g) + H_2O.$$

Additionally, the products (gypsum) of this reaction can react with the hydrochloric acid (HCl) to produce calcium chloride and sulfuric acid, creating a continuous interaction between the acids and the rock until equilibrium is obtained

$$2HCl(aq) + CaSO_4(s) \Rightarrow CaCl_2(aq) + H_2SO_4(aq).$$

The sulfuric acid solution and hydrochloric acid were injected into separate ports. The reactions of the sulfuric/hydrochloric acid solutions occurred in flow paths where the two solutions mix. The acidic solutions reacted in their own path until they reached a common path/channel. The dissolution and the precipitation were the factors expected to alter the geometry of the fracture, i.e., to affect the mechanical and hydraulic properties of the fracture.

For Rock 2, after the chemical alteration, a solution of solid spherical silica beads (average diameter of 25 microns) was flowed through the fracture. The bead solution consisted of 0.23 grams of silica beads per 100 ml of water. The aqueous solution of beads was injected into the sample using the same method as that used for the chemical flow but with a higher head (height). This solution simulated sand transport in fractures.

2.6. Fluid Flow Measurements. To understand the relationship between the seismic and hydraulic properties of the fracture, flow rates were measured. A falling head method was used to measure flow rates through the fracture plane. The flow rates were measured using distilled water. A burette (4000 ml) was filled with water and connected to the fracture sample by Tygon tubing. The output of the fracture was measured in grams using a Metter PM6100 electronic scale and in milliliters using burettes. The outflow was measured as a function of time. From the flow measurements, an average aperture can be calculated. Brown [16] showed that hydraulic conductivity is locally proportional to the cube of the aperture. The "cubic law" that relates aperture to volumetric flow rate is

$$b_{ap}^3 = \frac{12\upsilon}{\rho g}\frac{Q\Delta L_{fp}}{w\Delta h} \tag{2.9}$$

where Q is the flow rate, g is acceleration due to gravity, υ is the viscosity, ρ is the density of the water, Δh is the burette drop, ΔL_{fp} is the linear path length inside the fracture (port to port distance), w is the diameter of the flow ports, and b_{ap} is the average fracture aperture. Based on equation (2.9), volumetric flow rate data were used to estimate the average aperture of the fracture.

3. DATA ANALYSIS.

3.1. Seismic Data. A coherent sum of the signals at each probe scale was used to determine if measurements from a small scale result in the same interpretation of fracture properties as those made on a larger scale. The coherent sum (C) consists of summing all the signals (S(t)) for a given scale and then dividing by the number of signals, N

$$C(t) = \frac{1}{N}\sum_{i}^{N} S_i(t) \tag{3.1}$$

For example, for the 2 mm scale (N=1600 signals), all of the signals were summed and divided by the number of signals. For the probe scale of 5 mm, N = 16 signals were used, and N = 4 signals were used for the 20 mm scale. The 60 mm probe scale used only one signal, therefore a coherent sum was not used. To make the comparison, the coherent sum at each scale was shifted in time to remove system delay differences and to align the first peak.

The dominant frequency of the signals was extracted using a wavelet transformation analysis [17]. The dominant frequency is the frequency at which the maximum amplitude of the group wavelet transform occurs. The error in choosing the dominant frequency is ±0.05 MHz (step-size in the frequency analysis). Transmission coefficients as a function of frequency were also determined from the information provided by the wavelet analysis. The signal spectrum at the arrival time that coincides with the maximum amplitude was determined for each signal for each sample. The spectra from the rock samples were normalized by the spectrum from the intact sample to produce the transmission coefficient. The transmission coefficient, T(ω), was used in equation (3.2) to calculated an effective fracture specific stiffness, κ, as a function of frequency, ω,

$$\kappa(w) = \frac{wZ}{2\sqrt{\left(\frac{1}{T(w)}\right)^2 - 1}} \tag{3.2}$$

where Z is the acoustic impedance defined by the product of the phase velocity and density. For our analysis, we used a phase velocity of 4972 m/s (measured velocity in the laboratory for non-fractured Limestone) and a density of 2360 kg/m^3. The acoustic impedance for the Limestone samples used in this study is 11.73 $\times$ 10^6 kg/m^{2}s.

4. RESULTS.

4.1. Intact Sample Results. The intact acrylic sample was used as a control sample because it is homogeneous and contains no fractures or micro-cracks. The Intact sample was used to quantify the repeatability of the seismic measurements of transmitted amplitude made using the lens system. The error in the measured transmitted amplitude across the fracture as a function of field-of-view is listed in Table 2.3 and is on the order of 5%.

Figure 6 shows the coherent sums for the three field-of-view datasets as well as that from the acoustic mapping dataset for the intact sample. The signals were shifted in time to align the first peaks for comparison. By comparing the period of the first cycle, it is observed that the frequency content of the signal is approximately the same on all scales for the intact sample (see also Figure 11b). From the wavelet analysis, the coherent sums from the 15 mm, 30 mm and 60 mm field-of-views exhibited a maximum frequency of 0.71 MHz (± 0.02 MHz) and at the 2mm scale a frequency of 0.73 MHz (± 0.02 MHz). Therefore, the acoustic lens system does not affect the frequency content of the signal within the experimental error. However, the amplitude of the signals is affected. These systematic effects are accounted for in the analysis by normalizing the data from the rock samples by the data from the intact sample.

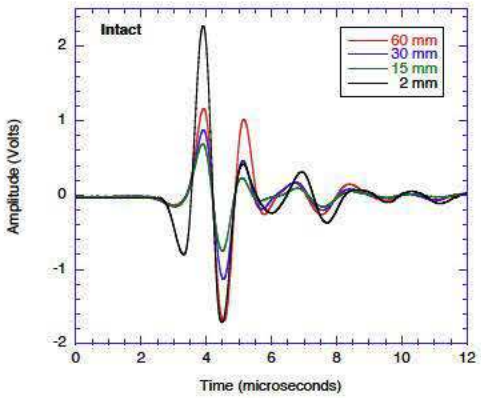

FIG. 6. *Coherent sum of received compressional waves for the intact acrylic sample. The acoustic map (2mm) signal is in black. The seismic measurements as a function of field-of-view are given for: 60 mm (red), 30 mm (blue) and 15 mm (green).*

4.2. Results from Rock Samples.

4.2.1. Flow Rates. Volumetric flow rates were measured for the fracture in Rock 1 and the fracture in Rock 2 (Table 4.1). Rock 1, which had two ports (180° apart), exhibited an increase in flow rate after the HCL solution flowed through the fracture. The flow rate through the fracture increased 32%. This suggests that the acidic solution enlarged the aperture of the fracture. Assuming a cubic relationship (equation 2.9) between flow rate and aperture, the average aperture increased by 60 microns from 430 microns to 490 microns.

For Rock 2, which had eight ports (45° apart), the volumetric flow rates were measured for a combination of diametrically opposite ports. The combinations of ports are referred to as (inlet to outlet): 5-1, 6-2, 7-3 and 8-4. The sulfuric acid solution was introduced into the fracture through port 5 and the hydrochloric solution was introduced into port 3 to create the HCL and H_2SO_4 solution. During the chemical invasion, ports 7, 8 and 1 were left opened to allow CO_2 produced by the reaction to escape. The sand solution was injected through port 8 and the only outlet was through port 4. After the two alteration processes (reactive flow & sand tansport), the flow rates from (a) ports 5-1 and 7-3 were similar to that of the initial condition, (b) port 6-2 increased relative to the initial condition, and (c) port 8-4 were smaller than the initial flow rates (Table 4.1). Reactive flow tended to increase the flow rate through all port combinations, while sand transport decreased the flow rate through all port combinations except 5-1.

The 6-2 port combination was perpendicular to the sand deposition process and were not used for chemical invasion of the reactive solutions. Using the cubic law (equation 2.9), the average aperture for all port combinations are listed Table 4.2. The 6-2 port combination was found to have increased by roughly 1 mm after all alterations. The proximity of ports 6 and 2 to the ports used for reactive flow (ports 5 and 3) may have caused the large increase of the flow rates for this port combination. The reactive flow altered the average aperture for all port combinations. Based on the flow measurements, the chemical solutions etched the fracture. The decrease in the 8-4 port combination was due to the sand transport process, i.e. the silica beads filled the voids in this flow path because these ports were used for the injection of the beads. Only for the 5-1 port combination did sand transport result in an increase in the flow rate and an increase in aperture.

4.2.2. Acoustic Mapping Results. The two-dimensional acoustic maps obtained using the acoustic mapping method described in Section 2.2 provided information on the local variations in fracture specific stiffness for the fractured rock samples. Figures 7 & 8 show the acoustic transmission maps for the Rock 1 and Rock 2, respectively. The acoustic transmission maps are the ratio of the signal amplitude for the fractured samples normalized by the signal amplitude from the Intact

	Initial Flow Rate (m^3/s)	Reactive Flow Rate (m^3/s)	Final Flow Rate (m^3/s)
Rock 1	$4.09 \pm 0.16 \times 10^{-8}$		$5.39 \pm 0.16 \times 10^{-8}$
Rock 2 Ports 5-1	$3.12 \pm 0.02 \times 10^{-6}$	$3.34 \pm 0.02 \times 10^{-6}$	$3.50 \pm 0.07 \times 10^{-6}$
Rock 2 Ports 6-2	$1.78 \pm 0.02 \times 10^{-6}$	$4.23 \pm 0.02 \times 10^{-6}$	$3.26 \pm 0.03 \times 10^{-6}$
Rock 2 Ports 7-3	$1.00 \pm 0.02 \times 10^{-6}$	$1.26 \pm 0.02 \times 10^{-6}$	$0.95 \pm 0.03 \times 10^{-6}$
Rock 2 Ports 8-4	$2.64 \pm 0.02 \times 10^{-6}$	$4.62 \pm 0.02 \times 10^{-6}$	$1.13 \pm 0.08 \times 10^{-6}$

TABLE 4.1

Volumetric flow rates for sample Rock 1 and Rock 2. Initial flow rates were measured for the water saturated condition for both samples. Reactive flow rates were measured for both samples but Rock1 is shown in the final condition. For Rock 2 the final condition is after the sand transport.

	Initial Average Aperture (mm)	Reactive Average Aperture (mm)	Final Average Aperture (mm)
Rock 1	0.430		0.490
Rock 2 Ports 5-1	4.64	4.75	4.84
Rock 2 Ports 6-2	3.84	5.19	4.72
Rock 2 Ports 7-3	3.16	3.41	3.10
Rock 2 Ports 8-4	4.38	5.30	3.88

TABLE 4.2

The average aperture calculated by using the flow rates given in Table 3 and equation (2.9) for samples Rock 1 and Rock 2.

sample. The color scales in Figures 7 & 8 are proportional to the transmission coefficients. Figures 7a&b show the transmission maps for the initial and final conditions for Rock 1. By comparing Figures 7 & 8, the effect of the reactive flow on the local fracture properties contains both local increases and local decreases in transmission. Reduced transmission is caused by chemical erosion of the fracture, while enhanced transmission is caused by the deposition of the end products of the reaction, i.e. calcium chloride.

Figure 8 shows the acoustic transmission maps for the initial and final conditions for Rock 2. After reactive flow followed by sand transport, transmission across the fracture increased across the entire area that was mapped. The transmission coefficients range between 1% to 5% for Rock 2 for both the initial and final conditions, which are much smaller than those observed for Rock 1 which ranged between 10%-80%. The low transmission coefficients exhibited by Rock 2 are consistent with the higher flow rates (i.e., larger apertures) observed for Rock 2 compared to Rock 1 (see Tables 4.1 & 4.2). Low transmission is associated with low fracture specific stiffness and high flow rates [8].

4.2.3. Coherent Sum Signals and Frequency Content.

4.2.3.1 Rock 1

Figure 9 is an example of seismic data obtained as a function of field-of-view by using the acoustic lens system on Rock 1 in the initial condition. One signal represents the 60 mm (Figure 9c), while 4 signals and 16 signals represent the 30 mm (Figure 9b) and 15 mm (Figure 9a) scales, respectively. These signals were collected in the same region but probed different subsets of the region (see Figure 5). Differences in arrival times, amplitudes and frequency content depend on the sub-region that was probed. One trend is the decrease in the amplitude from the large field-of-view to the small field-of-view, because the collection area decreases as the field-of-view decreases.

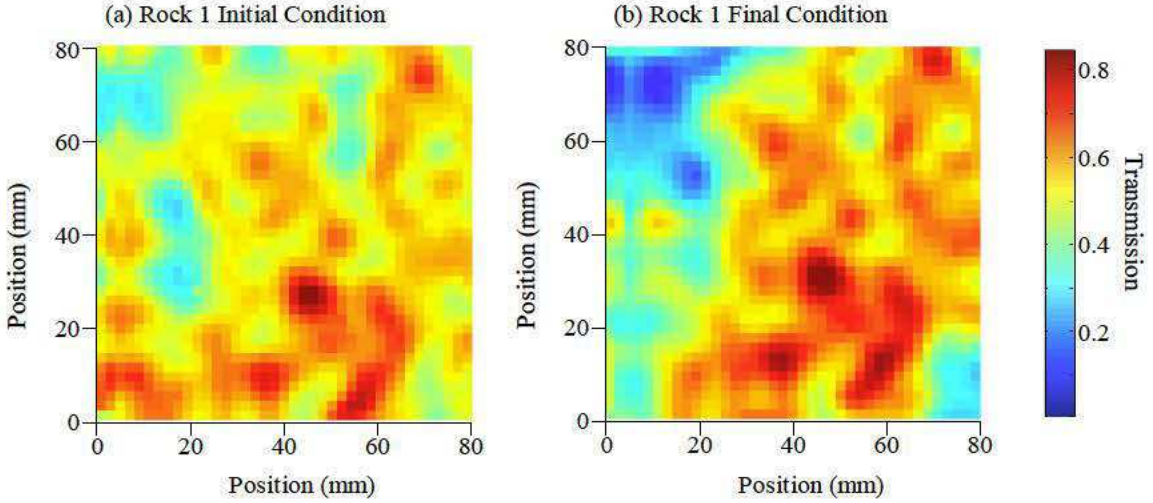

FIG. 7. *Transmission as a function of position for Rock 1 for (a) the initial condition and (b) the final condition. The total area scanned was 80 mm by 80 mm in 2 mm increment. The color scale to the right indicates the ratio of the transmitted compressional wave amplitude through the fractured sample to that through the acrylic sample.*

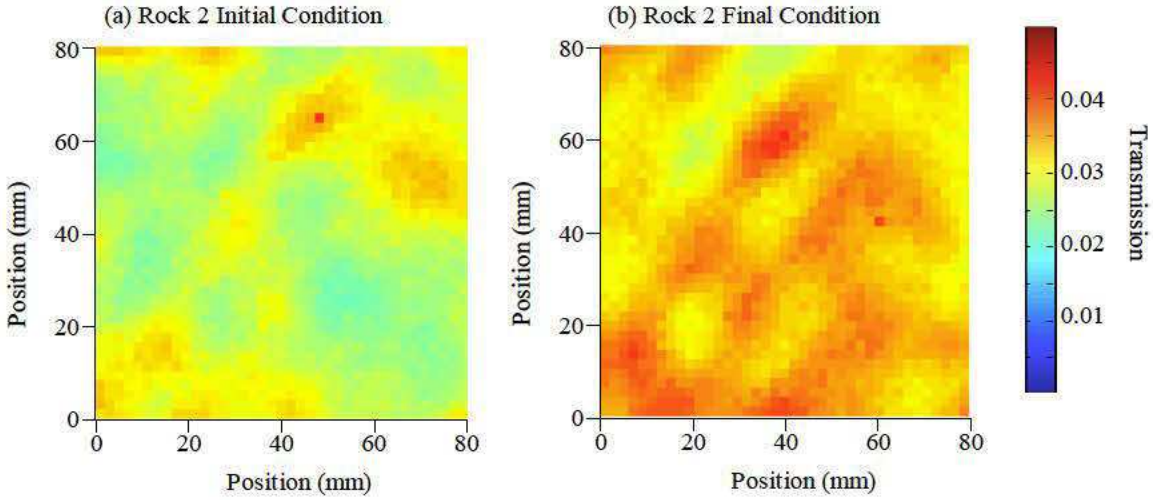

FIG. 8. *Transmission as a function of position for Rock 2 for (a) the initial condition and (b) the final condition. The total area scanned was 80 mm by 80 mm in 2 mm increment. The color scale to the right indicates the ratio of the transmitted compressional wave amplitude through the fractured sample to that through the acrylic sample.*

The coherent sums of the signals from Rock 1 shown in Figures 9a&b are given in Figure 10a as a function of field-of-view. The signals have been shifted in time to align the first peaks to enable a direct comparison of the amplitude and frequency content of the signal. For Rock 1 in the initial condition (Figure 10a) the coherent sums have approximately the same frequency for the 2 mm, 15 mm and 60 mm field-of-view scales. This was confirmed by the wavelet analysis, which found that the frequencies for these field-of-views ranged between 0.51 MHz to 0.59 MHz (Fig. 11b). Only the coherent signal from the 30 mm scale exhibited a significantly different frequency (0.41 MHz). From the histogram (Figure 11a) of the dominant frequency obtained from the 1600 signals on the 2 mm,

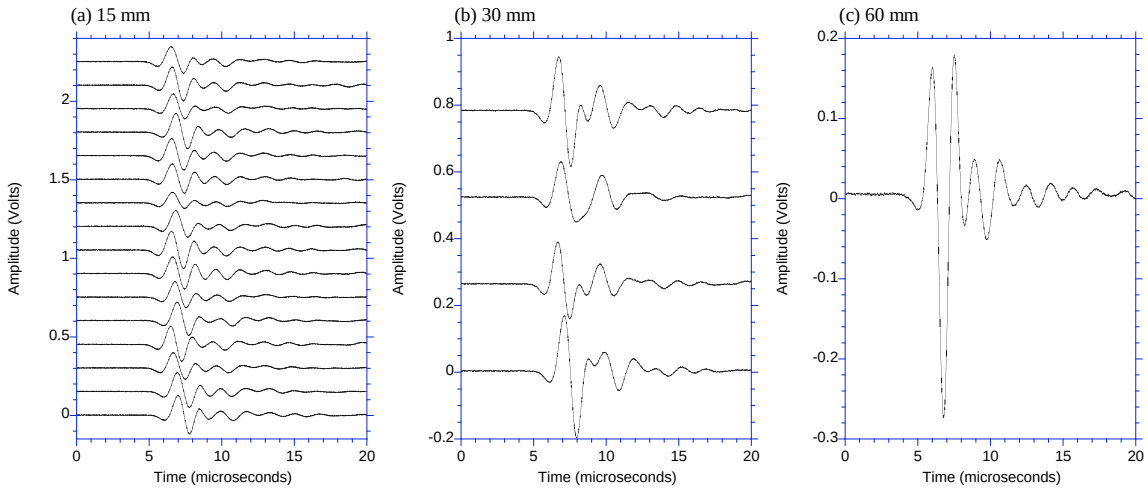

FIG. 9. *Received compressional waves transmitted through sample Rock 1 in the initial condition for field-of-views (a) 15 mm, (b) 30 mm, and (c) 60 mm. The systematic time delayed associated with the acoustic lens method is not included in the time base.*

it is inferred that the fracture in Rock 1 is relatively uniform, i.e. the probabilistic distribution of the dominant frequency is very narrow.

After reactive flow, the signals from Rock 1 in the final condition (Figure 10b) decreased in amplitude and the dominant frequency also decreased (Figure 11a). The histogram of the dominant frequency for Rock 1 (final condition) is observed to shift to slightly lower frequencies and the width of the distribution decreased compared to that from Rock 1 in the initial condition (Figure 11a). The decrease in the width of the distribution indicates that the fracture has become more uniform.

The narrowing of the width of a frequency distribution was observed by Gilbert and Pyrak-Nolte [18] for single fractures in a granite rock in which calcium carbonate was precipitated by the mixing of two solutions within a fracture. They observed a shift of the frequency distribution to high frequencies as well as a decrease in the width (variance) of the frequency distribution. In Gilbert and Pyrak-Nolte [18], the homogenization of the fracture, (i.e., with mineral precipitation), coincided with a decrease in flow rate. In our current study, the decrease in the width of the frequency distribution for Rock 1 also indicates homogenization of the fracture plane, but the flow rates increased after the reactive flow and the probabilistic distribution shifted to lower frequency. Equation (3.2) was used to determine the specific stiffness of the fracture in Rock 1 prior to and after reactive flow. Fracture stiffness was calculated as a function of frequency by using the coherent sum signals for the 2mm, 15 mm, 30 mm and 60 mm scales (Figure 12a). In all bout the 2 mm scale, the fracture specific stiffness decreased after reactive flow. This is consistent with the observed increase in flow rate and the shift in the probabilistic distribution of the dominant frequency to lower values after reactive flow.

Based on the work of Pyrak-Nolte & Nolte [9], frequency-dependent stiffness indicates the homogeneity or lack of homogeneity of the probability distribution of fracture specific stiffness. When the field of view was small (2 mm – 15 mm), the fracture specific stiffness in Figure 12a is relatively constant with frequency, i.e. the fracture is behaving as a displacement discontinuity [12]. As Pyrak-Nolte & Nolte [9] demonstrated theoretically, a frequency-independent fracture specific stiffness arises when the fracture has a uniform probabilistic distribution of stiffness. However, as the field of view increases to 60 mm, the fracture specific stiffness becomes frequency dependent which occurs when a fracture contains a non-uniform probabilistic distribution of stiffnesses. The change in the functional relationship between fracture specific stiffness and frequency with change in

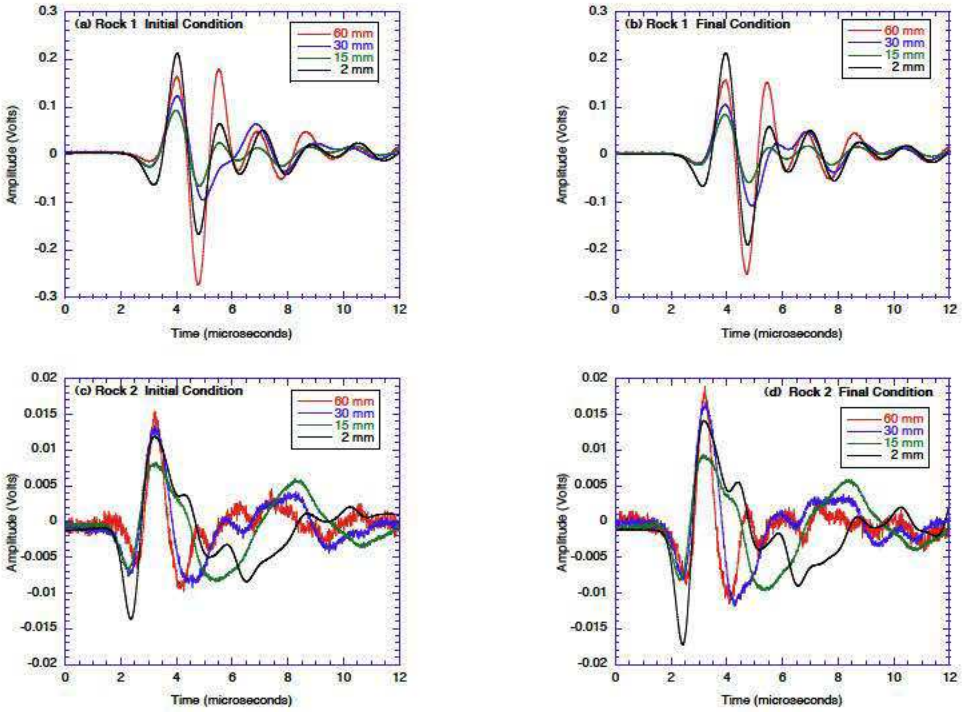

FIG. 10. *A comparison of the coherent-sum signals for (a) Rock 1 in the initial condition, (b) Rock 1 in the final condition, (c) Rock 2 in the initial condition, and (d) Rock 2 in the final condition for four field-of-views. The signals have been shifted in time so that the first positive peak of the signal at each field-of-view is aligned. The acoustic map (2mm) signal is in black. The seismic measurements as a function of field-of-view are given for: 60 mm (red), 30 mm (blue) and 15 mm (green).*

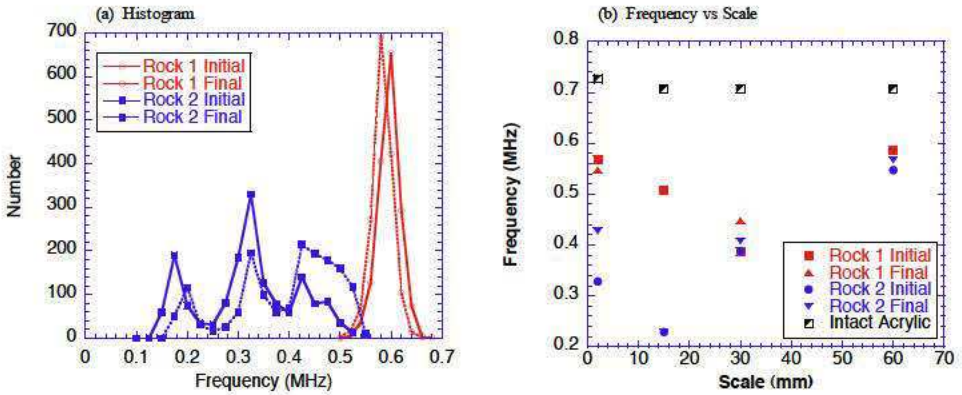

FIG. 11. *(a) Histogram of dominant frequency for Rock 1 and Rock 2 in the initial and final conditions from the 1600 waveforms collected on the 2 mm scale. (b) The dominant frequency obtained from the coherent signals as a function of scale (i.e., field-of-view).*

field-of-view is caused by a spatial distribution of fracture specific stiffness. When the field-of-view is small, the wavefront illuminates only a small region of the fracture. In this small region, the fracture specific stiffness may be relatively uniform. However, as the field of view increases to 60 mm, the beam encounters a spatial distribution of fracture specific stiffness, resulting in a fracture specific stiffness that increases with increasing frequency. The frequency dependence is a good indicator of the degree of homogeneity of the fracture specific stiffness. A change in the frequency dependence

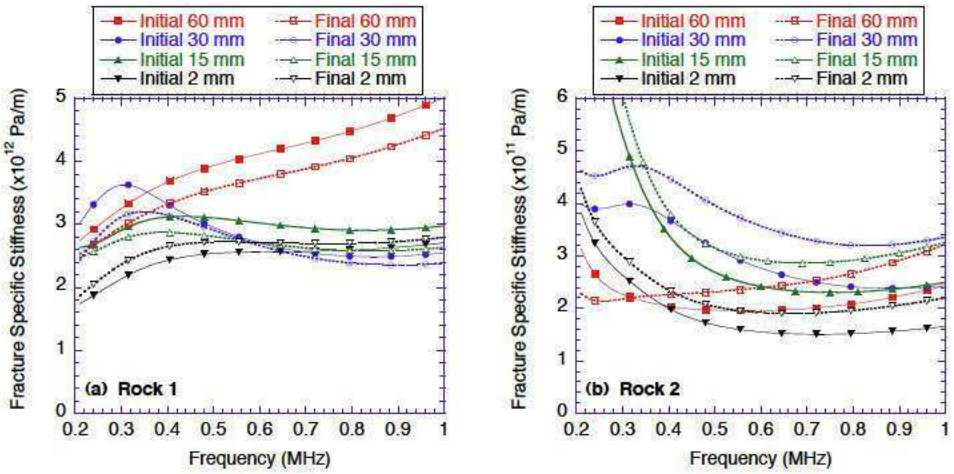

FIG. 12. *Effective fracture specific stiffness as function of frequency for samples (a) Rock 1 and (b) Rock 2 as a function of field-ofview for initial (solid lines) and final (dashed lines) conditions. The acoustic map (2mm) result is shown in black, and the field-of-view results are show in red (60 mm), blue (30 mm) and green (15 mm).*

with field-of-view is a good indicator of a spatial distribution in fracture specific stiffness. From the analysis, we estimate a spatial correlation length of the fracture specific stiffness that is on the order of 30 mm for the fracture in Rock 1, which is when the fracture specific stiffness changes from being relatively frequency-independent to being frequency dependent (Figure 12).

4.2.3.2 Rock 2

Rock 2 is a weakly-coupled fracture that has a larger average aperture than Rock 1 and exhibits a lower fracture specific stiffness (Table 4.2 & Figure 12). The frequency distribution for the fracture in this sample is not as homogeneous as for Rock 1. The histogram of the dominant frequency from the 2 mm scale is tri-modal for Rock 2 (Fig. 11a), while the frequency of the 15 mm, 30 mm and 60 mm scale increase with increasing field-of-view (Figure 11b). The high-frequency components of the signal were scattered out of the field-of-view for the 15 mm and 30 mm scales. On the other hand, the scattered signal components are captured on the 60 mm scale because the lens is collecting signals from larger scattering angles. The scattering losses are most likely associated with diffraction from the fracture. For Rock 2, the seismic measurements from the small scale cannot be simply scaled up to the large scale (60 mm) because of the change in the frequency content of the signals (Figures 10c&d and 11) with scale.

The volumetric flow rates through Rock 2 (Table 4.1) are consistent with fracture apertures on the order of 1-5 mm. At 1 MHz, the wavelength of the signal is comparable to some of the apertures in the fracture, resulting in strong scattering. This is confirmed from an examination of the fracture specific stiffness as a function of frequency for Rock 2 in Figure 12b. As noted earlier, when the seismic response of a fracture is within the displacement discontinuity regime, the fracture exhibits either a fracture specific stiffness that is frequency independent (if the stiffness distribution is uniform) or the fracture specific stiffness increases with increasing frequency (if there is a probabilistic distribution of fracture stiffness, and if the asperity spacing is smaller than a wavelength). For Rock 2 at field-of-view scales of 2 mm, 15 mm and 30 mm, the fracture specific stiffness decreases with increasing frequency for frequencies up to 0.5 MHz. Above this frequency, the curves flatten out. On the other hand, for the 60 mm scale, the stiffness increases slightly with frequency. The stiffness distribution for the fracture in Rock 2 produces a seismic response that is a mixing of regimes. Rayleigh scattering causes the stiffness to decrease with increasing frequency because the high frequency components of the signal are scattered out of the collecting field-of-view. The narrower angles for the smaller fields of view eliminate the high frequencies. Therefore, the fracture specific stiffness is not frequency dependent at higher frequencies than 0.5 MHz for

this sample. On the other hand, the part of the fracture response behaving as a displacement discontinuity causes the fracture specific stiffness to increase slightly with increasing frequency. A balance between these two regimes is only observed on the 60 mm scale because it is the only scale able to collect the scattered energy. It is only by comparing the frequency-dependent behavior of fracture specific stiffness as a function of field-of-view that enables the discrimination of the existence of the two scattering regimes, i.e., Rayleigh scattering and displacement discontinuity behavior. Identification of multiple scattering regimes provides information on the geometric properties of the fracture relative to the wavelength and improves seismic characterization of the mechanical and hydraulic properties of a fracture.

5. Conclusions. The ability to interpret fracture properties from seismic data is intimately linked to an understanding of the role of probabilistic and spatial distributions in fracture specific stiffness. Fracture specific stiffness is a function of the asperity distribution within a fracture as well as the size of the fracture apertures. Both of these geometric properties prevent single-point measurements on the small scale to be used to interpret fracture properties over a large scale. For example, Rock 1 was found to have a relatively uniform fracture specific stiffness when the field-of-view (the portion of the fracture illuminated by the wavefront), was small (for 2 mm and 15 mm). Only on the larger scales (60 mm) was a spatial and probabilistic distribution of fracture specific stiffness inferred. Also, as observed for Rock 2, a range of geometric scales cause a mixed seismic response because of overlapping scales. Parts of the fracture may behave as a displacement discontinuity ($\lambda >$ asperity spacing or aperture) while other areas of the fracture may produce strong scattering ($\lambda \leq$ asperity spacing or aperture). In our experiments, it was our ability to change the field-of-view that enabled us to determine that the fracture response was a mix of scattering regimes. Understanding the effect of overlapping length scales on seismic wave propagation across fractures is important for correctly interpreting fracture properties.

The results from this study have important implications for interpreting seismic data on the laboratory scale as well as on the field scale. For example, in the laboratory, measurements made on the 15 mm to 30 mm scale are compatible with the diameter of the piezoelectric crystal in the transducers. If measurements are only made at these scales, the interpretation of fracture properties or bulk properties may be difficult or misleading if the sample produces strong scattering. In turn, many small-scale local measurements of the seismic response of a fracture cannot be directly summed and averaged to predict the global (large scale) response of the fracture because of scattering losses outside the field-of-view. The key to understanding the seismic response on any scale is to examine the fracture specific stiffness both as a function of frequency and as a function of field-of-view. As observed in our experiments, how fracture specific stiffness changes or remains constant with frequency helps determine if a uniform or non-uniform probabilistic distribution of fracture specific stiffness is present, and also if scattering regimes are involved. In the characterization of a fracture from seismic measurements, frequency independent fracture specific stiffness is not sufficient to establish the homogeneity of the fracture. This study showed that 21 measurements over three scales (i.e., field-of-views) were needed to unravel the competing effects of spatial correlations and probability distributions in Rock 2. Measurements obtained from different field-of-views enable the estimation of the spatial correlation length in fracture specific stiffness.

Quantifying fracture specific stiffness using seismic data is important for remotely sensing fracture properties and monitoring alteration in these properties from time-dependent processes. The relationship between fluid flow and fracture specific stiffness is an important interrelationship because measurements of seismic velocity and attenuation can be used to determine remotely the specific stiffness of a fracture in a rock mass. If this relationship holds, seismic measurements of fracture specific stiffness can provide a tool for predicting the hydraulic properties of a fractured rock mass. Currently, no analytic solution exists to link flow and fracture specific stiffness and is most likely statistical in nature [19]. However, it has been shown numerically [8] that the relationship between fluid flow and fracture specific stiffness arises directly from the size and spatial distribution of contact area and void space within a fracture. The acoustic len method for adjusting field-of-

view demonstrated that information on spatial distributions in fracture properties is achievable from seismic measurements.

Acknowledgments. The authors wish to acknowledge support of this work by the Geosciences Research Program, Office of Basic Energy Sciences US Department of Energy (DEFG02-97ER14785 08). Also AAC acknowledges the Rock Physics Group at Purdue University for the help during this work.

REFERENCES

[1] Pyrak-Nolte, L.J., C.D. Montemagno, and D.D. Nolte, *Volumetric imaging of aperture distributions in connected fracture networks*. Geophysical Research Letters, 1997. 24(18): p. 2343-2346.
[2] Brown, S.R., R.L. Kranz, and B.P. Bonner, *Correlation between surfaces of natural rock joints*. Geophysical Research Letters, 1986. 13: p. 1430-1434.
[3] Brown, S.R. and C.H. Scholz, *Closure of random surfaces in contact*. Journal of Geophysical Research, 1985. 90: p. 5531.
[4] Hopkins, D.L., *The Effect of Surface Roughness on Joint Stiffness, Aperture and Acoustic Wave Propagation*. 1990, University of California, Berkeley: Berkeley.
[5] Hopkins, D.L., N.G.W. Cook, and L.R. Myer. *Fracture stiffness and aperture as a function of applied stress and contact geometry*. in 28th US Symposium on Rock Mechanics. 1987. Tucson, Arizona: A. A. Balkema.
[6] Kendall, K. and D. Tabor, *An ultrasonic study of the area of contact between stationary and sliding surfaces*. Proc. Royal Soc. London, Series A., 1971. 323: p. 321-340.
[7] Johnson, J., S.R. Brown, and H.W. Stockman, *Fluid flow and mixing in rough-walled fracture intersections*. Journal of Geophysical Research, 2006. 111(B12206): p. doi:10.1029/2005JB004087.
[8] Pyrak-Nolte, L.J. and J.P. Morris, *Single fractures under normal stress: The relation between fracture specific stiffness and fluid flow*. International Journal of Rock Mechanics and Mining Sciences, 2000. 37(1-2): p. 245-262.
[9] Pyrak-Nolte, L.J. and D.D. Nolte, *Frequency-Dependence of Fracture Stiffness*. Geophysical Research Letters, 1992. 19(3): p. 325-328.
[10] Schoenberg, M., *Elastic wave behavior across linear slip interfaces*. Journal of the Acoustical Society of America, 1980. 5(68): p. 1516-1521.
[11] Gu, B.L., K.T. Nihei, L.R. Myer, and L.J. Pyrak-Nolte, *Fracture interface waves*. Journal of Geophysical Research-Solid Earth, 1996. 101(B1): p. 827-835.
[12] Pyrak-Nolte, L.J., L.R. Myer, and N.G.W. Cook, *Transmission of Seismic-Waves across Single Natural Fractures*. Journal of Geophysical Research-Solid Earth and Planets, 1990. 95(B6): p. 8617-8638.
[13] Dunn, F. and F.J. Fry, *Acoustic elliptic lenses - an historical note*. Journal of the Acoustical Society of America, 1980. 68(1): p. 350-351.
[14] Jaeger, J.C. and N.G.W. Cook, *Fundamentals of Rock Mechancis*. 1972, London: Methuen & Co, KTD.
[15] Singurindy, O. and B. Berkowitz, *Evolution of the hydraulic conductivity by precipitation and dissolution in carbonate rock*. Water Resources Research, 2003. 39(1): p. 1016.
[16] Brown, S.R., *Fluid flow through rock joints: The effect of surface roughness*. Journal of Geophysical Research, 1987. 92: p. 1337-1347.
[17] Nolte, D.D., Pyrak-Nolte, L. J., Beachy, J., and C. Ziegler, *Transition from the displacement discontinuity limit to the resonant scattering regime for fracture interface waves*. International Journal of Rock Mechanics and Mining Sciences, 2000. 37(1-2): p. 219-230.
[18] Gilbert, Z., and L. J. Pyrak-Nolte, *Seismic monitoring of fracture alteration by mineral deposition*. in 6th North American Rock Mechanics Symposium. 2004. Houston, Texas.
[19] Jaeger, J.C., N.G.W. Cook, and R. Zimmerman, *Fundamentals of Rock Mechanics*, 4th Edition. 2007: Wiley-Blackwell.